JATIS Journal of Astronomical Telescopes, Instruments, and Systems

RESEARCH PAPER

Arcus X-ray telescope performance predictions and alignment requirements

Hans Moritz Günther[a,*] **Peter Cheimets**[b] **Casey T. DeRoo**[c] **and Ralf K. Heilmann**[a,d]

[a]MIT Kavli Institute for Astrophysics and Space Research, Cambridge, Massachusetts, United States
[b]Harvard-Smithsonian Astrophysical Observatory, Center for Astrophysics, Cambridge, Massachusetts, United States
[c]University of Iowa, Department of Physics and Astronomy, Iowa City, Iowa, United States
[d]MIT Kavli Institute for Astrophysics and Space Research, Space Nanotechnology Laboratory, Cambridge, Massachusetts, United States

ABSTRACT. Arcus is a concept for a National Aeronautics and Space Administration probe-class X-ray mission to deliver high-resolution Far Ultraviolet and X-ray spectroscopy with two separate instruments. We focus on the X-ray spectrograph (XRS). It consists of four spectral channels arranged in a double-tilted Rowland torus geometry. It combines cost-effective silicon pore optics with high-throughput critical-angle transmission gratings to achieve at least $R > 3000$ in a bandpass from 12 to 50 Å. We present ray-tracing studies to derive performance characteristics such as the spectral resolving power and effective area and look at the best positioning of the four channels to improve the resiliency toward misalignments and reduce the overall impact of chip gaps. We study the effect of misalignments on the performance and present alignment requirements in 6 degrees of freedom for all optical elements in the XRS. We conclude that most tolerances can be achieved with mechanical means alone.

Keywords: Arcus; ray-tracing; tolerances; alignment; X-ray

Paper 24062SS received May 9, 2024; revised Sep. 11, 2024; accepted Sep. 23, 2024; published Oct. 16, 2024.

1 Introduction

High-resolution X-ray and ultraviolet (UV) spectroscopy open a window into the physics of the universe that often cannot be observed with any other technique. X-rays and UV can probe the hottest and most ionized gas that remains invisible in longer wavelengths because the high ionization levels do not produce observable transitions in the radio, infrared, or optical. Thus, observations in the UV and X-rays probe the most energetic processes in a number of systems. A few examples are stellar space weather;[1] the accretion onto young stars, where the UV and X-rays come from the energetic infall of material from the disk onto the stellar surface; the innermost regions of the accretion disks around black holes; and the absorption of background (X-ray) light from distant, bright continuum sources by the warm–hot inter-galactic medium to find the missing baryons.[2,3] High-resolution UV and X-ray spectroscopy that resolves the profiles of individual emission or absorption lines is particularly valuable because it allows us to address a host of physical questions that cannot be answered by simply measuring the broad-band X-ray flux. To follow up with one specific example, in the case of accretion onto young stars, resolving the

*Address all correspondence to Hans Moritz Günther, hgunther@mit.edu

2329-4124/2024/$28.00 © 2024 SPIE

kinematic line profile of emission in different ions can tell us which part of the emission is formed in the infalling, red-shifted accretion column; which part is related to the stellar corona seen at the rest wavelength of the star (possibly with small velocities from up and downflows in the corona); and which part is formed in (or possibly absorbed by) the blue-shifted outflow.[3]

The Arcus mission is a concept that will address those challenges with two instruments for X-ray and UV high-resolution spectroscopy. The mission evolved through several stages. It was originally proposed as an instrument mounted on the International Space Station[4] and then redesigned as a satellite.[5,6] Arcus' X-ray spectrograph (XRS) will perform high-resolution spectroscopy in the soft X-ray range (~12 to 50 Å) with a resolving power $R > 3000$ or better and an effective area $A_{\mathrm{eff}} > 200$ cm^2 for most of the bandpass with a peak of $A_{\mathrm{eff}} > 550$ cm^2 around 18 Å. The resolving power is a factor of 3 to 5 larger than what existing instruments on Chandra or X-Ray multi-mirror mission (XMM)-Newton can deliver, and the effective area is also significantly higher; the exact number depends on the bandpass, e.g., in the crucial region around the O VII He-like triplet, which is density and temperature sensitive, Arcus will reach about two orders of magnitude more effective area than the High Energy Transmission grating (HETG) on Chandra currently has. The UV spectrograph is described by Ref. 7, and the UV science case is discussed by Ref. 8. In this work, we concentrate on the XRS.

Beginning in the very early phases of the mission design, we performed ray-tracing to verify the performance characteristics of Arcus and to improve the design;[9] in particular, in Refs. 10 and 11, we utilized ray-tracing to determine the allowable misalignments of the mechanical elements that make up Arcus. Ray-tracing is particularly well suited for the problem because it allows an arbitrary misalignment to be introduced for any element in the optical path, and it can quickly iterate over different input parameters. Since the work in Ref. 10, the XRS concept has evolved yet again: the number, size, and location of the silicon pore optics (SPO) modules have changed to match the current design of the Athena Observatory.[12] We presented an update on that in a conference proceeding in Ref. 11, and the purpose of this publication is to bring updated calculations of the XRS into the peer-reviewed literature.

2 Layout of the X-ray Spectrograph on Arcus

The XRS on Arcus follows the layout of a double-tilted Rowland spectrograph (DTRS). This concept is described in detail in Ref. 13 and summarized in this section. We first discuss the general geometry, channel placement, and position of the detectors in Sec. 2.1 because they are shared among all channels. Then, we describe the SPO (Sec 2.2) and gratings (Sec. 2.3) that are specific to each channel.

Spectrographs with a single Rowland torus consist of a focussing X-ray mirror, gratings positioned on one side of the torus, and detectors on the other. The spectrum is dispersed perpendicular to the optical axis, and the narrowest focus in the dispersion direction is located where the rays reach the opposite side of the torus. The intersection of the torus with the plane of the optical axis and dispersion direction is called the "Rowland circle."[14] The optical axis can pass through the center of the torus, or the torus can be tilted with respect to the optical axis. The DTRS combines two tori, tilted in opposite directions and arranged such that their Rowland circles overlap. This allows the dispersed light from both tori to be imaged onto the same set of detectors. Figure 1 shows a conceptual drawing of a DTRS with two channels.

2.1 Double-tilted Rowland Torus layout

In the XRS, each Rowland torus is tilted by 3.6175 deg, about twice the blaze angle.[13,15,16] This number is set such that the distance between two channels matches the space required to mount the grating petals next to each other. At the same time, all channels can be imaged on the same set of detectors (Fig. 3). Two cameras are positioned to capture the zeroth order on one side and the blaze peak on the other. There is a gap between the two cameras because so little signal is found in that region that it is not useful to capture it with charge-coupled devices (CCDs).

In the XRS, each of the two channels of the DTRS is split into two parts, so that there are four channels in total, see Fig. 2 for a rendering of a ray-trace. Two of them have the zeroth order on the left in Fig. 3 and disperse to the right, and two of them have the zeroth order on the right and disperse toward the left. The pair of channels dispersing in the same direction sets the critical-angle

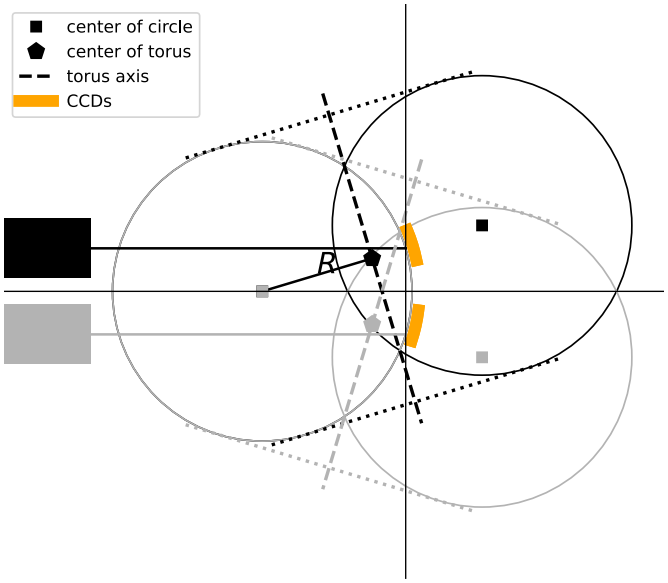

Fig. 1 Conceptual drawing of a double-tilted Rowland torus layout with two channels. Each channel has its own Rowland torus (black and gray in the figure), which dictates the placement of mirrors, diffraction gratings, and detectors. This drawing shows a cut through a plane that contains the optical axes (horizontal) and the diffraction direction (vertical). Each 3D torus is obtained by rotating the circles around the corresponding dashed axis. Dotted lines are shown to help guide the eye for this 3D structure. The tori are positioned such that they overlap in one circle ("Rowland circle," the circle on the left side of the figure). This circle determines the location of the detectors, and thus, both channels can be imaged onto the same set of detectors. Arcus uses a variation of this concept where each of the two channels is split into two parts for a total of four channels; this is explained in the text and later figures. Similar figures with more detail can be found in Ref. 13.

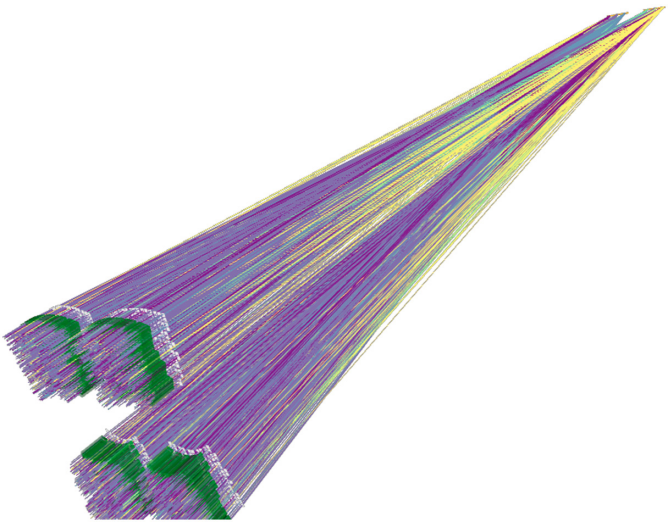

Fig. 2 Ray-trace of a monochromatic spectrum in the XRS. In the bottom left of the image are the four independent channels with SPO (green) and CAT gratings (white). Rays converge on the detector (top right). Purple rays are the zeroth order, and other colors are different dispersed orders. The two leftmost channels position the zeroth order on the left set of detectors and disperse toward the right, and the two rightmost channels position the zeroth order on the right detectors and disperse toward the left.

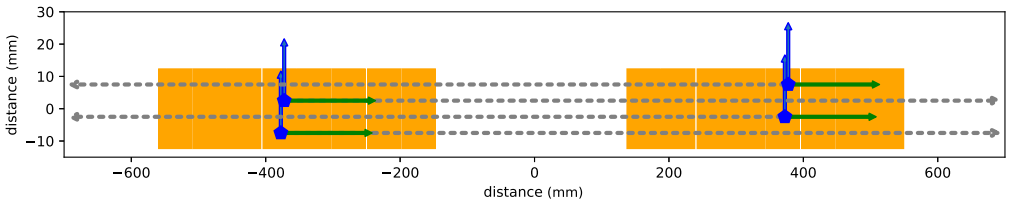

Fig. 3 Layout of the CCDs (orange rectangles) in the focal plane. Given the resolution of the figure, most chip gaps are not visible. Also note that the *x*- and the *y*-axes are scaled differently. Two cameras with eight CCDs each are located in the focal plane. In this plot, 0 is the geometric center of all the Rowland tori involved. Note that the cameras are intentionally not symmetric to 0. The position of the four optical axes for the four channels is marked with a blue pentagon. The dispersion (*x*—green horizontal arrows) and the cross-dispersion (*y*—blue vertical arrows) of the different spectra are parallel to each other and point in the same direction. Two channels disperse left-to-right and two right-to-left as indicated by the dashed arrows corresponding to each channel.

transmission (CAT) gratings on very similar Rowland tori, which are offset from each other in cross-dispersion direction by 10 mm so that the signal is clearly separated on the CCDs. They are also offset from each other in dispersion direction by 5 mm to ensure that the same wavelength seen in different channels falls onto different x coordinates on the CCDs, and thus, a wavelength that happens to be lost in a chip gap between two CCDs in one channel can be observed in the other channel. This split also means that there is no need to align all channels to the same zero-order position within the width of the point-spread function (PSF) (less than 1.5 arcsec in dispersion direction). See Ref. 17 in this special issue for details on the detectors and the camera design.

2.2 Silicon Pore Optics

SPOs are a technology developed and matured for Athena.[18] They provide a large effective area at a relatively low weight and cost.[12,19,20] In Arcus, the SPO petals use "sub-aperturing," which means that the SPOs do not cover a full circle but only a narrow wedge. That provides Arcus with an asymmetric PSF that is only ∼1.5 arcsec wide in the dispersion direction. It also means that the individual petals where the SPO are mounted are not circular, but roughly rectangular, and four separate panels (one per optical channel) can fit into the front assembly of the telescope.

2.3 Critical-Angle Transmission Gratings

CAT gratings are manufactured at the Space Nanotechnology Laboratory. Progress on the development, manufacturing, and X-ray performance of CAT gratings is given in a series of papers stretching back many years.[21–25] Reference 26 in this special issue describes the details of the CAT gratings for the XRS. CAT gratings have a very high aspect ratio, where the grating bars are ∼90 times higher than they are wide. Arcus will feature CAT gratings with a period of 200 nm in the dispersion direction, 140-nm gaps between the bars, and a depth of 5.7 μm. The gratings are manufactured with sizes up to 32×32 mm^2. Individual grating bars are held in place by a perpendicular support structure of wider Si bars (L1 support) and a hexagonal frame (L2 support) that the gratings bars and L1 supports rest on. The L2 mesh blocks ∼19% of the area, and the recently fabricated L1 meshes block between 10% and 18%.

CAT gratings are mounted blazed, which means that the grating bars are not perpendicular to incoming rays but tilted by 1.8 deg. Together with the high aspect ratio, this leads to absolute diffraction efficiency >30% at 2.38 nm wavelength (sum over orders 3 to 8), including absorption by L1 and L2 supports.[27] In this setup, the photons are mostly diffracted into one direction, the so-called blaze peak at twice the blaze angle—see Fig. 4 for a schematic. Four to six CAT gratings are bonded into a window for each SPO. Those windows are then arranged into a grating petal for each channel.

3 Ray-traces

We study the performance and alignment requirements of Arcus with ray-tracing. We use the ray-tracing code MARXS,[28,29] a Python code developed by us under an open source license. MARXS

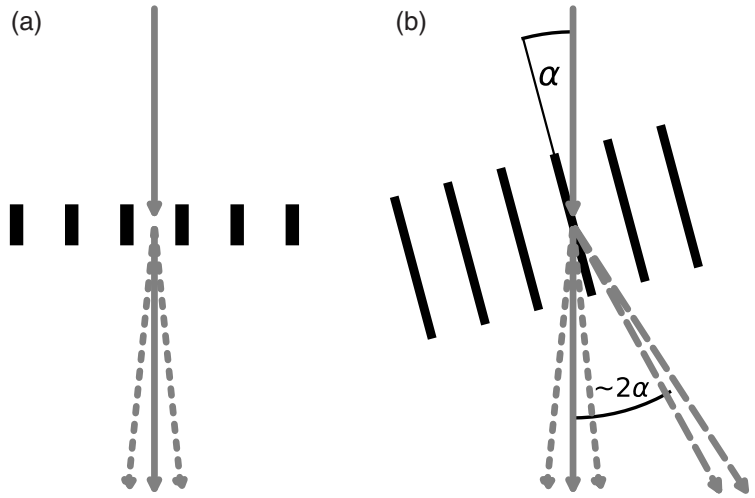

Fig. 4 Schematic for a diffraction grating mounted perpendicular to the incoming rays (traditional transmission grating) (a) and a CAT grating mounted blazed (b) with a blaze angle α. Direct light (order zero) is shown as an arrow and low orders (-1 and $+1$) are shown as dashed arrows. The blazed grating has a higher diffraction efficiency, and the photons are mostly diffracted into one direction, the so-called blaze peak at about (depending on the wavelength and the position of diffracted orders) twice the blaze angle (dotted arrows); at higher energies (dashed arrows), the CAT grating sidewall no longer reflect the rays, and the photons end up in the zeroth order or low-diffraction orders (-1 and $+1$).

is available at https://github.com/chandra-marx/marxs; simulations in this article are done with version 2.0. MARXS has been used for several mission proposals and is backed by hundreds of unit tests and verified against laboratory works and on-orbit Chandra observations where feasible. MARXS does not calculate material properties such as reflectivities or grating efficiencies; instead, they are read from tables that can be based on laboratory data or simulations calculated by other programs.

For SPO, we use a description that is fast to calculate and that we can easily tune to the observed or expected performance of the SPO. Instead of a three-dimensional (3D) structure, we define a single flat plane. When rays pass that plane, we look where a photon would have gone if it had been a central ray (i.e., the focal point for an on-axis source). We then re-direct our photon to that point. For an on-axis source, this prescription would bring all rays to the focal point exactly; for an extended source, it creates a sharp image in the focal plane. Obviously, the PSF is not a point, so we add, at the point of the intersection with the plane and after redirecting the ray, two random angles to the ray direction: one in the plane of reflection and one in the perpendicular direction. Those two angles are randomly drawn from Gaussian distributions with widths that are chosen to reproduce measured or prescribed PSF shapes. This simple prescription gives us rays with the right spread in direction to propagate to the gratings without the need to know the details of the figure errors in the SPO plates that cause that scatter. We consider the geometric opening area (including ribs) and angle-dependent reflectivity to predict the effective area, but this prescription does not reproduce the vignetting or off-axis effects on the PSF.

Efficiencies for the CAT gratings are an input to MARXS. They are calculated using rigorous coupled-wave analysis for a wide range of energies and angles. Those efficiencies are then scaled to match measurements at synchrotron facilities and other beamlines, which are done only for a few energies and angles due to time constraints.[30] The numbers include the effect of cross-dispersion from L1 support structures, dispersion, and blockage by the hexagonal L2 supports, and any coverage by grating frames.

The cameras are covered by a contamination-blocking filter of 30-nm Al deposited on 45-nm polyimide and held by a thicker mesh with 95% transmission. The mesh is treated statistically in the ray-trace as a 5% reduction in intensity; 40-nm Al deposited directly on the detectors block optical light. The transmission for Al and polyimide is taken from Ref. 17 with the X-ray absorption fine structure for *C* edge from measurements of Chandra advanced CCD imaging spectrometer (ACIS) imaging filter.[31] For the quantum efficiency of the CCD, we follow the quantum

efficiency of the Suzaku XIS1 BI CCD assuming depletion depth 42 μm[32] because the CCDs baselined for Arcus are also manufactured by the Massachusetts Institute of Technology (MIT) Lincoln Laboratory and have the same pixel size, number of pixels per segment, gate structure, and operating voltages.

4 Effective Area and Resolving Power

The main performance characteristics of Arcus are the effective area and the resolving power of the extracted spectra. We run simulations on a wavelength grid from 1.5 to 60 Å in steps of 0.15 Å. Each simulation is run with 100,000 rays. MARXS tracks the probability of survival for each ray; for example, when a ray passes a filter that transmits 15% of the photons at that energy, the probability of that ray reaching the detector is multiplied by 0.15. In the end, the sum of the probabilities of all rays hitting the detector divided by the total number of rays simulated for a given entrance aperture gives the effective area with much lower statistical noise than in codes where photons either pass or do not pass individual elements. We estimate that the uncertainty on the Arcus performance is dominated by systematics. The statistical uncertainty for each run is below a few percent. To get an order of magnitude for the systematics that we expect, we look at observatories such as Chandra, XMM-Newton, and others currently in flight where the relative difference in the effective area among different instruments is typically 5% to 20%.[33]

The effective area for Arcus is shown in Fig. 5 and the spectral resolving power R per order and averaged over all dispersed orders that are detected at a particular wavelength (weighted by the effective area of each order at that wavelength) in Fig. 6. In the actual data analysis, orders will be extracted into separate datafiles and be fitted jointly to make use of the full R and A_{eff} in each order. However, for the purpose of discussing alignment tolerances later in this paper, we can simplify this to an average R because the orders that contribute most strongly to the signal typically have similar R values anyway (e.g., at 23 Å order -6 and -7 contribute with an R that differs by <20%). The figure distinguishes among the photons seen in dispersion and in order zero, i.e., in direct light, where the only energy resolution is provided by the CCD. The effective area in direct light is high for high energies, in particular, including the 6.7 keV (1.85 Å) iron line, which is a crucial diagnostic in many astrophysical sources; but even at these energies, some photons are diffracted to order 1 and -1 because the gratings act as phase-shifting gratings.

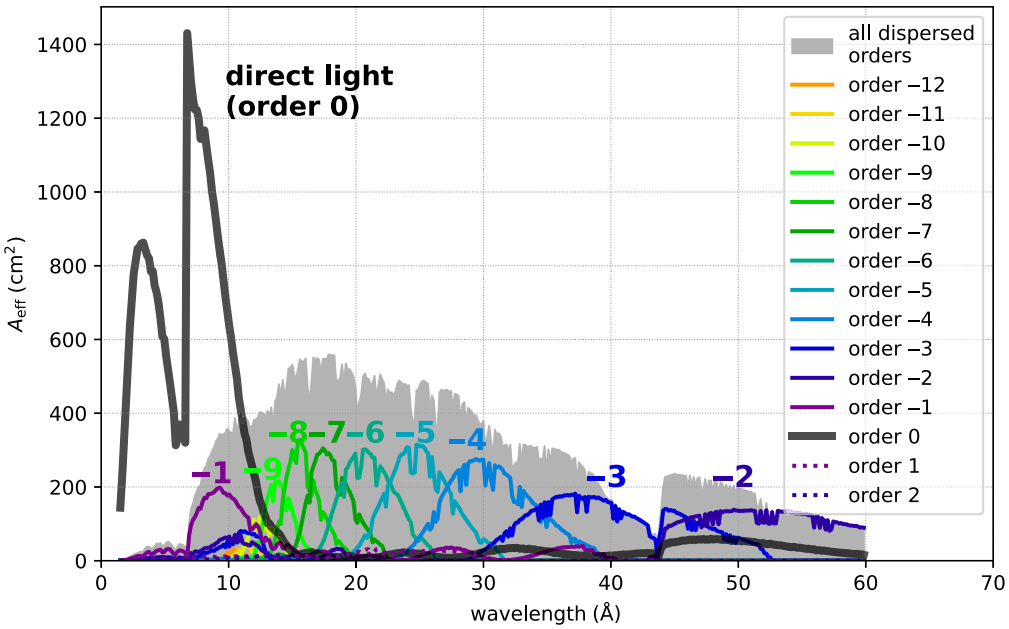

Fig. 5 Effective area for Arcus based on ray-trace simulations. The effective area of individual dispersion orders is shown. Order numbers are listed in the legend, and the strongest order is also labeled in the plot itself. For most wavelength ranges, several dispersed orders contribute to the total effective area.

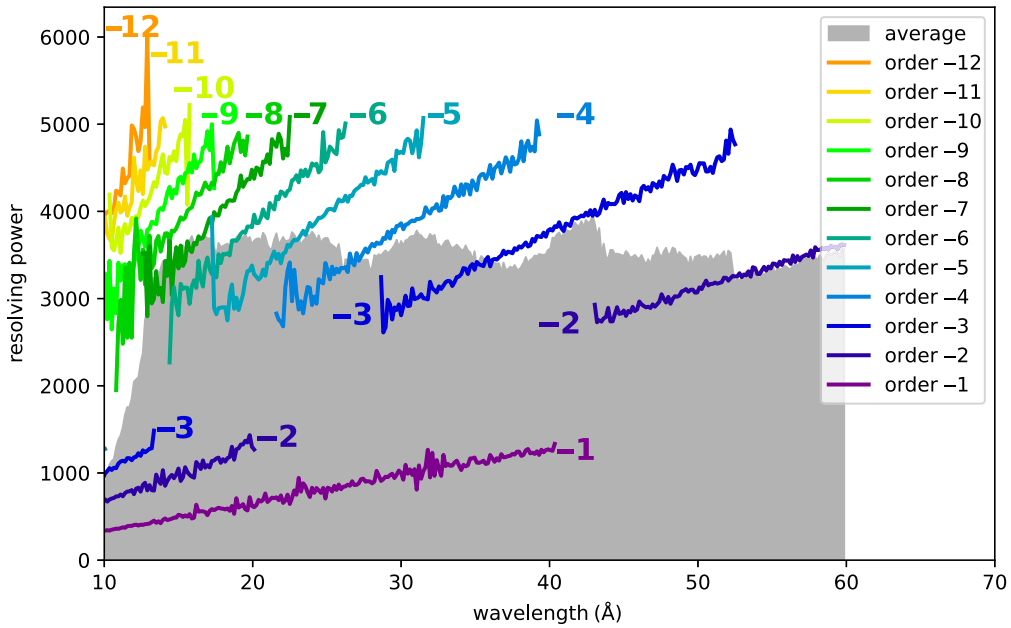

Fig. 6 Resolving power R for Arcus. Colored lines show R per order, and order numbers are shown in the legend and the plot itself. The gray area shows R averaged over all diffracted orders contributing to that wavelength, where the average is calculated weighting each order by the effective area. For low orders, there are gaps in the colored lines. At low wavelength, those orders fall on the same camera as the zeroth order, e.g., for order −2 up to 20 Å. In order −2, photons longer than 43 Å are dispersed into the blaze peak and detected on the other camera.

Toward longer wavelengths, around 10 Å, there is a significant signal in order 1 and −1 with R of a few hundred. From ∼12 to 60 Å, most photons are dispersed into the blaze peak on the set of detectors opposite of the zeroth order and Arcus achieves an average R of around 3500. The resolving power increases with increasing distance between the location of the zeroth other and the dispersed signal. For a given order, that means that R increases with wavelength. However, for most wavelengths, multiple orders contribute to the signal. As the wavelength increases, the order on the far side of the blaze peak becomes weaker, and orders on the near side stronger, such that the average R is approximately constant.

Depending on the flux and spectrum of the source, science users may choose to extract only a limited set of the available data. This would reduce the available effective area. For example, for weak sources in regions with high background, weak orders might be contaminated too much to be useful, or one might choose a spatially smaller extraction region to reduce the background at the cost of also loosing some source photons. Also, several dispersed orders will be located at the same location on the chip and must be separated using the CCD energy resolution, and there will be some contamination among orders. Although this normally can be considered in the data analysis, in some cases, it might be beneficial to use a more conservative scheme that reduces cross-order contamination at the cost of some effective area. These effects are discussed in detail in Ref. 34.

5 Alignment Tolerances

We use ray-traces to assess the effect of misalignments on the performance of Arcus. Science requirements put limits on the maximal allowable degradation of spectral resolving power and effective area, and engineering constraints determine how well, e.g., individual SPO can be aligned into petals, how well the petals can be aligned to the forward assembly, and how well the forward assembly can be aligned to the detector housing. In general, tighter tolerances require more work, time, and money. We thus need to understand how important each possible degree of freedom is to the total performance of the system to identify those where significant design and work need to go into the alignment.

The simulations start from a perfectly aligned version of Arcus. Even this does not provide infinite resolving power, because the model includes a pointing jitter, a limited PSF, some

astigmatism inherent in the design, and finite sizes of CAT gratings and CCD detectors, which means that they deviate from the ideal Rowland geometry. A ray-trace is run with this design, and spectral resolving power (R) and effective area (A_{eff}) are calculated.

After running the baseline version, one element of Arcus is shifted in 1 degree of freedom, e.g., all CCDs are shifted by 1 mm in the dispersion direction. The ray-trace is repeated, again R and A_{eff} are calculated, then all CCDs are shifted by 2 mm and so on. After testing out the parameter space in the dispersion direction, the CCDs will be shifted in a cross-dispersion direction. In this way, each element (for example, the CCD array) will be misaligned by various amounts in one of 6 degrees of freedom (shift along x, y, and z and rotation around x, y, and z). In the Arcus coordinate system, the z-axis is parallel to the optical axis, the x-axis is the grating dispersion direction, and the y-axis is the cross-dispersion direction. Unless noted, rotations are not done around the origin of the coordinate system but around the center of an element (e.g., the center of an SPO petal).

In the first stage, only 1 degree of freedom is changed at a time because it is not computationally feasible to explore the entire parameter space. From those results, we identify where the alignment is easily (e.g., just from simple machining tolerances) much better than the requirements. In the second step, we can then run ray-traces where all degrees of freedom are varied according to the misalignment budget and thus check if the assumptions going into combining the misalignments in different degrees of freedom hold or if non-linear interactions degrade R and A_{eff} more than expected. Should this be the case, we revise the misalignment budget appropriately.

To keep the computational load reasonable, we simulate only one channel of Arcus. As the spectra from each channel will be extracted separately and there is symmetry among the channels, most results apply equally to all channels. We discuss in the text the few instances where the channel symmetry does not apply. Each simulation consists of 200,000 photons and the same source photons are used for each series of ray-traces, e.g., all global CCD misalignments use the same photons.

Figures 7–9 show some examples of the results. In the figures, A_{eff} is given summed over all dispersed orders that fall on a CCD (bottom row), and R is the average resolving power, where

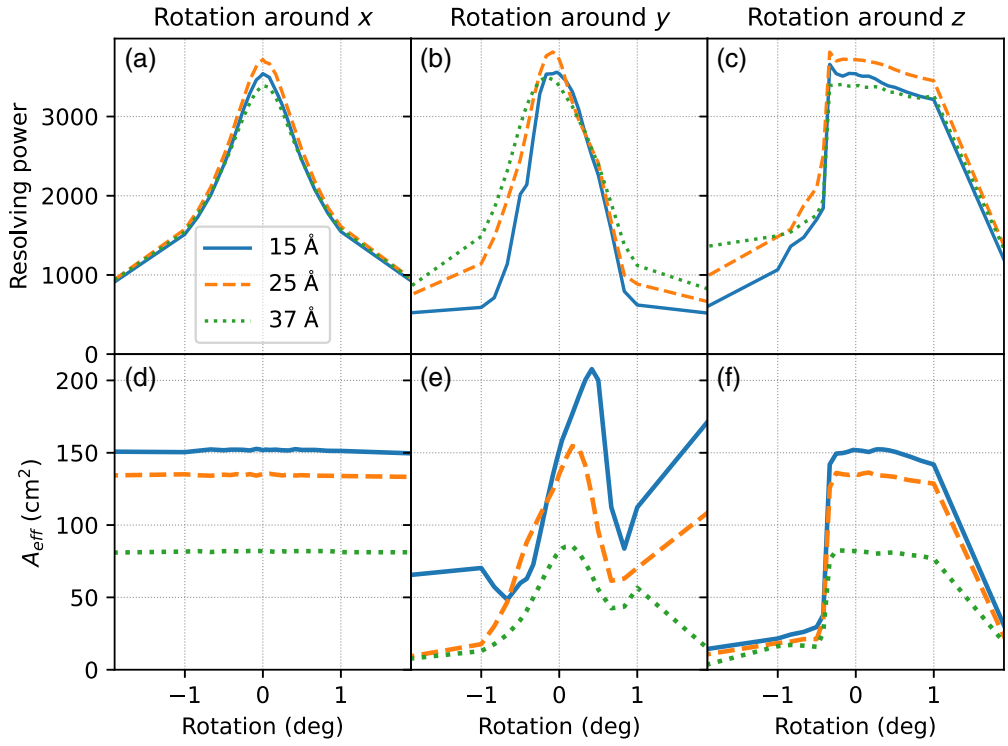

Fig. 7 Effect of misalignment of the CAT grating petal for rotation around the center of the petal. (a)–(c) Resolving power for rotation around x, y, and z, respectively. (d)–(f) Effective area for rotation around x, y, and z, respectively.

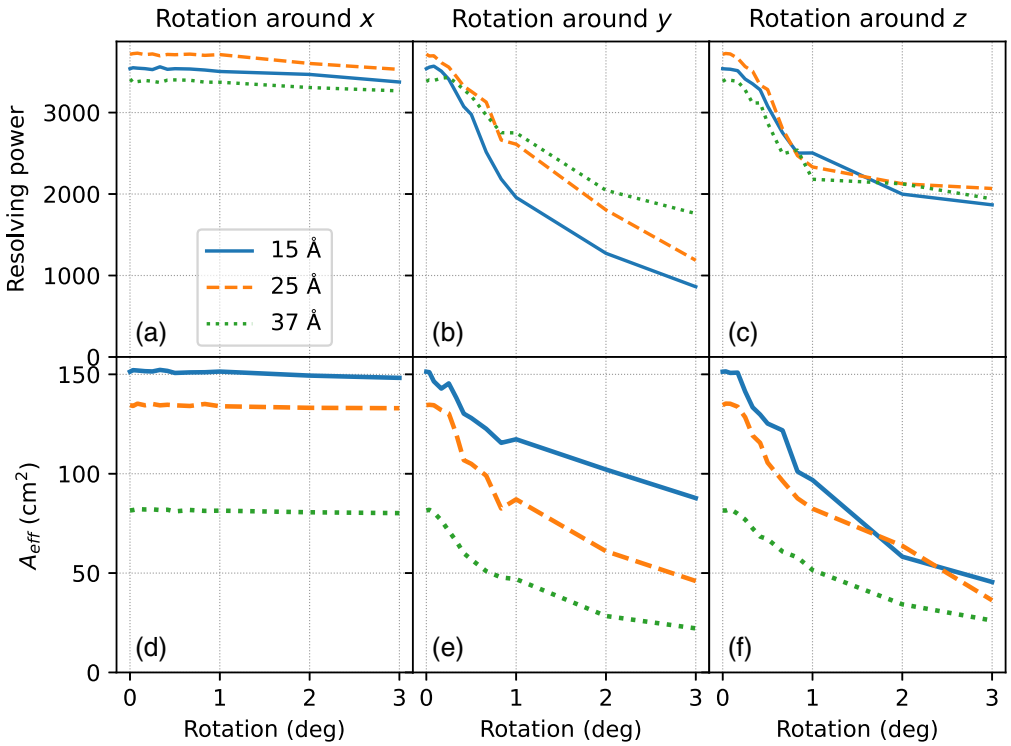

Fig. 8 Effect of misalignment of individual CAT gratings. The misalignment for each grating is drawn from a normal distribution, and the σ of that distribution varied from 0 to 3 deg. (a)–(c) Resolving power for rotation around x, y, and z, respectively. (d)–(f) Effective area for rotation around x, y, and z, respectively. Note that the A_{eff} reported is only for a single channel.

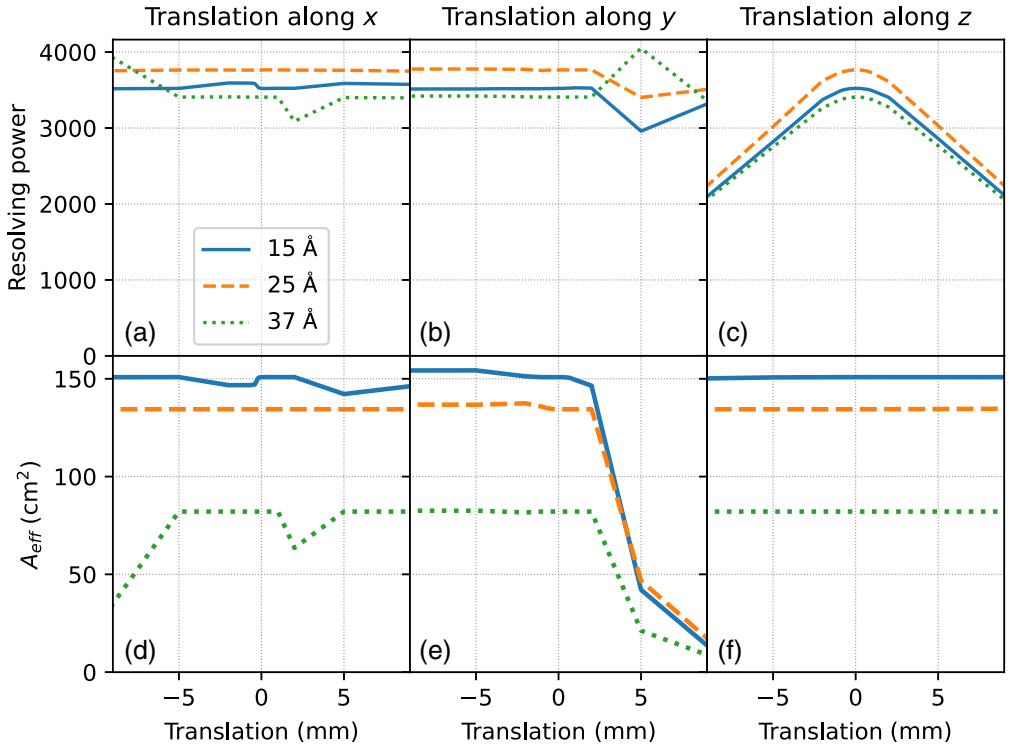

Fig. 9 Effect of misalignment of the cameras with respect to the front assembly. (a)–(c) Resolving power for translation parallel to x, y, and z, respectively. (d)–(f) Effective area for translation parallel to x, y, and z, respectively.

the resolving power from individual orders is weighted by the number of photons in that particular order (top row). Thus, it is possible that R in the plot increases with increasing misalignment if A_{eff} drops at the same time. This happens when an order with lower-than-average R drops off the CCD (thus reducing the summed A_{eff} and increasing the average R). There is no scientific benefit from the apparently increased R here—if one required a higher resolving power, the lower orders can be ignored in the scientific analysis even if they fall on the CCD.

Figure 7 shows the effect of a change in the CAT grating petal position, whereas the SPO petal and the cameras are fixed. Rotations around either x or y mean that the CAT gratings on one side move up, whereas the other side moves down, changing the path length of the diffracted photons. Those photons coming from the high CAT gratings travel further along the dispersion direction than those from the low gratings, thus causing the dispersed spot to smear out, which reduces R. These rotations need to be kept at the level of a few arcminutes. Rotation around z changes the direction of the dispersed light, and for large angles, the dispersed orders miss the CCD.

Figure 8 examines the rotations of individual gratings. For each grating in the CAT petal, a different misalignment is drawn from a normal distribution. Rotations around x (the dispersion direction, see panels (a) and (d) in the figure) have little effect on R. As the flat facets have finite size, their edges differ from the Rowland torus by a little already, and adding a little more rotation does not change much. Rotations in y quickly reduce A_{eff} though, because the CCDs are placed for a certain blaze peak. Rotating the CAT gratings shifts the blaze peak, and more photons end up in orders that are not captured by the CCDs. Rotation around z causes more and more signals to miss the detector. There is no sharp cutoff, because the CAT gratings in the simulation have a distribution of rotation angles, and the larger the Gaussian σ is, the more CAT gratings will send their dispersed photons to positions where they cannot be detected. From this figure, we can determine that the alignment tolerance for rotation around x can be large, whereas the other two directions are of order a few arcminutes to prevent significant degradation of the Arcus performance. It is one of the key advantages of working in a transmission rather than reflection grating geometry that even the most stringent alignment tolerances for a single arcsec PSF (in the dispersion direction) are on the order of several arcmin.

Figure 9 shows simulations for translating the detector with respect to the forward assembly (SPO and CAT gratings). The most important degree of freedom is a change in focus [panel (c)]. A shift along y has no impact, as long as it is small enough to keep the dispersed spectrum on the CCDs. For the particular channel simulated here, the spectrum drops off the CCDs for y shifts for ~ -15 mm on one side and about $+5$ mm on the other side. A shift of 5 mm or more will drop at least one channel of the detector.

The curves for changing R with shift in x show some up and down when an order hits a chip gap [panels (a) and (d)]. For example, two orders contribute to the signal in the curve for 37 Å photons. At $+2$ mm, one of them hits a chip gap, causing a drop in A_{eff} and also in R (R is averaged over all contributing orders, but only one order, which happens to have a lower R, is detected at this position). Note that chip gaps are inevitable. There will always be some wavelengths in a chip gap; however, the overall performance of the instrument, which is averaged over a range of wavelengths, is unaffected by this. Although a shift along x does matter in principle because the focal plane is curved, we find that shifts up to a few millimeters have little impact, as if the CCDs move in the dispersion direction, the spectrum will be only slightly out of focus. As described above, the Arcus design takes advantage of this to mitigate the effect of chip gaps by offsetting the different channels by a few millimeters in dispersion direction so that no two spectra have chip gaps at the same wavelength.

We run simulations for rotations and translations for each possible mechanical misalignment in Arcus, as well as for a few other parameters such as the SPO mirror PSF, the repeatability of the CAT grating period, and the surface flatness of the CAT gratings. As a first step, we inspect all results and determine a misalignment that degrades performance by roughly 10%. In some cases, it is obvious that mechanical placement alone will position the elements much better than that, e.g., if individual CAT gratings are rotated by several degrees with respect to each other, they will not fit into the grating petal. In this case, we assign a reasonable number for the misalignment in Table 1.

Table 1 Arcus alignment tolerances derived from ray-tracing (1σ).

Alignment	Trans x (mm)	Trans y (mm)	Trans z (mm)	Rot x (in.)	Rot y (in.)	Rot z (in.)
Individual SPO in petal	0.007	0.033	0.167	100	100	3
CAT petal to SPO petal	0.333	0.333	0.333	100	100	200
CAT windows to CAT petal	0.333	0.333	0.067	100	60	100
Individual CAT to window	0.333	0.333	0.067	100	60	100
Camera to front assembly	1.667	0.667	0.333	60	60	60

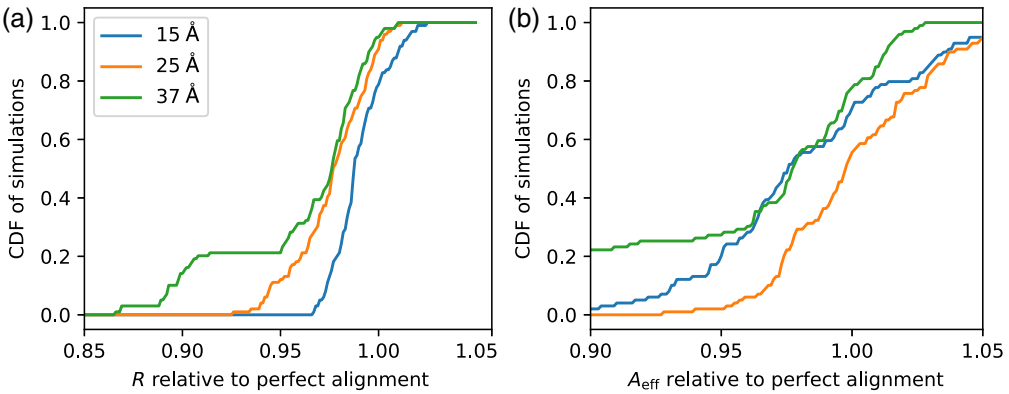

Fig. 10 Cumulative distribution function for R (a) and effective area (b) relative to a perfectly aligned Arcus for a set of simulations where all elements are simultaneously misaligned according to the misalignment budget in Table 1.

The alignment budget assumes that all alignment tolerances contribute independently. The next set of simulations is designed to check this assumption. Some misalignments might cancel out in practice, others might have a multiplicative effect. Full ray-tracing is the best way to check that and to predict final instrument performance. We run a set of 100 ray-traces and draw a new set of misalignments from Table 1 for each of them. Figure 10 shows the cumulative distribution of R and effective area for those simulations relative to a perfectly aligned Arcus.

Differences are visible among the different wavelengths. At 37 Å, two dispersed orders (order -3 and -4) contribute, but order -3 is close to the edge of a CCD, and order -4 is close to a chip gap. If either one is lost, R or A_{eff} at that wavelength will suffer, but at the same time, a neighboring wavelength will improve because it is no longer inside a chip gap. In contrast, the signal at 25 Å is dominated by order -6, comfortably in the middle of a CCD. Thus, the two plots above should not be interpreted as "longer wavelength will suffer more"; crucial orders are close to a chip gap in different spots over the Arcus bandpass. Instead, the plots should be read as showing the range of effects that the baseline misalignment can have on R and A_{eff}, depending on what exactly the random numbers are that are drawn. Apart from the effects of shifting chip gaps as in the 37 Å case, Fig. 10 shows that the alignment tolerances listed in Table 1 give us 95% of the nominal R and effective area in more than 90% of the realizations.

Table 1 then needs to be iterated with the mechanical design to see which degrees of freedom can easily be tighter (and thus will not significantly degrade the performance in any case), which degrees of freedom are impacted by the co-alignment among the different Arcus instruments, which can be corrected with more expensive or more time-consuming procedures or in-flight alignment mechanisms (see Ref. 35), and how much degradation in performance is acceptable to still reach the science goals of the mission. In that sense, Table 1 is a starting point for the alignment budget, though the final budget will be close to those numbers for most degrees of freedom. If an alignment is much tighter than the budget in the table, it does not improve the

overall performance, but if it is much looser, a single misalignment could reduce the performance below the science requirements.

6 Future Work

At this point, the main limitation of this work is our simplified mirror model. We expect it to work well for on-axis sources, but it does not reproduce the vignetting which becomes significant at ~2 arcmin off-axis. Our simplified mirror model also leads to a flat focal plane, whereas a Wolter–Schwarzschild optic typically has a slightly curved focal surface. Detailed ray-trace models specific to the Athena SPO are available[36–38] and can be coupled with our code for CAT gratings and detectors.

7 Summary

Arcus is a probe-class mission concept with two high-resolution spectrographs in the UV and in X-rays. The X-ray instrument (XRS) is designed in a double-tilted Rowland torus geometry with four channels with independent mirror and grating petals. All four channels are imaged onto the same set of detectors. We discuss the ray-racing model we set up for Arcus and describe the input data for mirrors, gratings, filters, and CCDs. We predict an effective area of >200 cm^2 from 8 to 50 Å with a peak of 550 cm^2 around 15 Å. The resolving power R is largely flat over the bandpass with $R > 3500$. Arcus will also detect higher-energy X-rays up to 10 keV in low diffraction orders (-1, 0, and $+1$) at the same time.

We run simulations to determine the alignment tolerances for Arcus. In many degrees of freedom, those are of order 0.5 mm for translations or 1 to 2 arcmin for rotations, which is easily achievable by mechanical means alone. Notably, the alignment requirements of individual SPO in a mirror petal and the translation of the CAT windows and petals along the optical axis are tighter and require dedicated alignment procedures.

Disclosures

The authors of this paper are members of the Arcus collaboration. Should the National Aeronautics and Space Administration (NASA) select Arcus for implementation, their institutions will receive funding which may be used to fund the author's salaries in full or in part in the future.

Code and Data Availability

We use the ray-tracing code MARXS,[28,29] a Python code developed by us under an open source license. MARXS is available at https://github.com/chandra-marx/marxs; simulations in this article are done with version 2.0. The database of efficiencies for gratings can be shared upon reasonable request by the Space Nanotechnology Laboratory - contact co-author Ralf Heilmann for access.

Acknowledgments

Support for this work was provided in part through NASA (Grant No. NNX17AG43G) and Smithsonian Astrophysical Observatory (SAO) contract SV3-73016 to MIT for support of the *Chandra* X-Ray Center (CXC), which is operated by SAO for and on behalf of NASA (Contract No. NAS8-03060). The simulations make use of Astropy, a community-developed core Python package for Astronomy,[39] numpy,[40] and IPython.[41]

References

1. N. S. Brickhouse et al., "An Arcus view of stellar space weather," *Astronomische Nachrichten* **343**, e20019 (2022).
2. L. W. Brenneman et al., "The evolution of structure and feedback with Arcus," *Proc. SPIE* **9905**, 99054P (2016).
3. R. K. Smith et al., "Arcus: the soft X-ray grating explorer," *Proc. SPIE* **11118**, 111180W (2019).
4. R. K. Smith et al., "Arcus: an ISS-attached high-resolution X-ray grating spectrometer," *Proc. SPIE* **9144**, 91444Y (2014).
5. R. K. Smith et al., "Arcus: the X-ray grating spectrometer explorer," *Proc. SPIE* **9905**, 99054M (2016).

6. R. K. Smith et al., "Arcus: exploring the formation and evolution of clusters, galaxies, and stars," *Proc. SPIE* **10397**, 103970Q (2017).
7. B. T. Fleming et al., "The Arcus ultraviolet spectrograph (UVS): technical design of the far-ultraviolet spectrograph on the Arcus probe," *Proc. SPIE* **12678**, 126780G (2023).
8. K. France et al., "Far-ultraviolet spectroscopy on the Arcus X-ray probe," *Proc. SPIE* **12678**, 126780F (2023).
9. H. M. Günther et al., "Ray-tracing critical-angle transmission gratings for the X-ray Surveyor and Explorer-size missions," *Proc. SPIE* **9905**, 990556 (2016).
10. H. M. Günther et al., "Ray-tracing Arcus in phase A," *Proc. SPIE* **10699**, 106996F (2018).
11. H. M. Günther et al., "Arcus X-ray telescope performance and alignment," *Proc. SPIE* **12678**, 126781D (2023).
12. M. J. Collon et al., "X-ray mirror development and production for the Athena telescope," *Proc. SPIE* **11852**, 118521Z (2021).
13. H. M. Günther et al., "Concept of a double tilted rowland spectrograph for X-rays," *ApJ* (submitted).
14. K. P. Beuermann, H. Bräuninger, and J. Trümper, "Aberrations of a facet-type transmission grating for cosmic X-ray and XUV spectroscopy," *Appl. Opt.* **17**, 2304–2309 (1978).
15. R. K. Heilmann et al., "Critical-angle transmission grating spectrometer for high-resolution soft X-ray spectroscopy on the international X-ray observatory," *Proc. SPIE* **7732**, 77321J (2010).
16. H. M. Günther et al., "Performance of a double tilted-Rowland-spectrometer on Arcus," *Proc. SPIE* **10397**, 103970P (2017).
17. C. E. Grant et al., "The focal plane of the Arcus probe X-ray spectrograph," *J. Astron. Telesc. Instrum. Syst.* **11**(1), 011007 (2024).
18. X. Barcons et al., "Athena: ESA's X-ray observatory for the late 2020s," *Astronomische Nachrichten* **338**, 153–158 (2017).
19. M. J. Collon et al., "Silicon pore optics development for ATHENA," *Proc. SPIE* **9603**, 96030K (2015).
20. D. Girou et al., "Silicon pore optics: a mature and adaptable X-ray mirror technology," *Proc. SPIE* **12679**, 1267905 (2023).
21. R. K. Heilmann et al., "Blazed high-efficiency X-ray diffraction via transmission through arrays of nanometer-scale mirrors," *Opt. Express* **16**, 8658 (2008).
22. R. K. Heilmann et al., "Diffraction efficiency of 200-nm-period critical-angle transmission gratings in the soft X-ray and extreme ultraviolet wavelength bands," *Appl. Opt.* **50**, 1364 (2011).
23. A. R. Bruccoleri, R. K. Heilmann, and M. L. Schattenburg, "Fabrication process for 200 nm-pitch polished freestanding ultrahigh aspect ratio gratings," *J. Vac. Sci. Technol. B* **34**, 06KD02 (2016).
24. R. K. Heilmann et al., "Demonstration of resolving power $\lambda/\Delta\lambda > 10{,}000$ for a space-based X-ray transmission grating spectrometer," *Appl. Opt.* **58**, 1223–1238 (2019).
25. R. K. Heilmann et al., "X-ray performance of critical-angle transmission grating prototypes for the Arcus mission," *ApJ* **934**, 171 (2022).
26. R. Heilmann et al., "Transmission grating arrays for the X-ray spectrometer on Arcus Probe," *J. Astron. Telesc. Instrum. Syst.* **11**(1), 011004 (2024).
27. R. K. Heilmann et al., "Blazed transmission grating technology development for the Arcus X-ray spectrometer explorer," *Proc. SPIE* **10699**, 106996D (2018).
28. H. M. Günther, J. Frost, and A. Theriault-Shay, "MARXS: a modular software to ray-trace X-ray instrumentation," *Astron. J.* **154**, 243 (2017).
29. H. M. Günther, J. Frost, and A. Theriault-Shay, "Chandra-marx/marxs: v2.0," Zenodo (2024).
30. R. K. Heilmann et al., "Flight-like critical-angle transmission grating X-ray performance for Arcus," *Proc. SPIE* **12181**, 1218116 (2022).
31. G. Chartas et al., "ACIS UV/optical blocking filter calibration at the National Synchrotron Light Source," *Proc. SPIE* **2805**, 44–54 (1996).
32. K. Koyama et al., "X-ray imaging spectrometer (XIS) on board Suzaku," *PASJ* **59**, S23–S33 (2007).
33. K. K. Madsen et al., "IACHEC cross-calibration of Chandra, NuSTAR, Swift, Suzaku, XMM-Newton with 3C 273 and PKS 2155-304," *Astron. J.* **153**, 2 (2017).
34. H. M. Günther, D. Huenemoerder, and E. D. Miller, "Order sorting and background handling for Arcus," *J. Astron. Telesc. Instrum. Syst.* **11**(1), 011006 (2024).
35. P. Cheimets et al., "Co-alignment methodology for the X-ray and UV spectrometers on Arcus Probe," *J. Astron. Telesc. Instrum. Syst.* **11**(1), (2024).
36. D. Spiga et al., "Simulation and modeling of silicon pore optics for the ATHENA X-ray telescope," *Proc. SPIE* **9905**, 99055O (2016).
37. G. Sironi et al., "Open-source simulator for ATHENA X-ray telescope optics," *Proc. SPIE* **11822**, 118220I (2021).
38. D. Spiga et al., "Modelling diffractive effects in silicon pore optics for the ATHENA X-ray Telescope," *Proc. SPIE* **12181**, 121814J (2022).

39. Astropy Collaboration et al., "The Astropy Project: sustaining and growing a community-oriented open-source project and the latest major release (v5.0) of the core package," *ApJ* **935**, 167 (2022).
40. S. van der Walt, S. C. Colbert, and G. Varoquaux, "The numpy array: a structure for efficient numerical computation," *Comput. Sci. Eng.* **13**(2), 22–30 (2011).
41. F. Pérez and B. E. Granger, "IPython: a system for interactive scientific computing," *Comput. Sci. Eng.* **9**, 21–29 (2007).

Hans Moritz Günther is a research scientist at Massachusetts Institute of Technology (MIT). He received his undergraduate degree (in 2005) and his PhD (in 2009) in physics from the University of Hamburg, Germany. After that, he worked at the Harvard-Smithsonian Center for Astrophysics and came to MIT in 2015. He is currently the lead developer of MARX, the ray-tracing software used for the Chandra X-ray Observatory. His science interests are in star formation using data from the radio to X-rays.

Peter Cheimets received his BS degree in mechanical engineering in 1978 from MIT and his MS degree in mechanical engineering with concentrations in dynamics and control systems from Stanford in 1981. He received his management of engineering degree from Tuft in 2007. He has developed astrophysical instrumentation for the Smithsonian Astrophysical Observatory since 1983, placing instruments on TRACE, Hinode, SDO, and IRIS, and is leading the effort to develop an instrument for MUSE.

Casey T. DeRoo received his BA degree in physics and classical studies in 2011 and his PhD in physics from the University of Iowa in 2016. He served as an Astrophysicist at the Smithsonian Astrophysical Observatory. He joined the faculty of the University of Iowa as an assistant professor in 2018 and was named a National Aeronautics and Space Administration Astrophysics Nancy Grace Roman Technology Fellow in 2020. His research interests include X-ray optics technologies, nanofabrication, and metrology.

Ralf K. Heilmann is a principal research scientist at the MIT Kavli Institute for Astrophysics and Space Research and is an associate director of the Space Nanotechnology Laboratory. He received his diploma in physics from the Friedrich-Alexander-Universität (FAU) Erlangen/Nürnberg (1991) and his MS (1993) and PhD (1996) degrees in physics from Carnegie Mellon University. After a postdoc at Harvard, he joined the SNL and has since focused on advanced lithography and the development of X-ray optics for astronomy.